MATERIALS CHEMISTRY FRONTIERS

CCS 中国化学会 CHINESE CHEMICAL SOCIETY

ICCAS

ROYAL SOCIETY OF CHEMISTRY

High Reactivity of Mesoporous CeO_2 to Dissociate Chemical Warfare Agent Sarin

Journal:	*Materials Chemistry Frontiers*
Manuscript ID	QM-RES-12-2022-001253.R1
Article Type:	Research Article
Date Submitted by the Author:	25-Feb-2023
Complete List of Authors:	Li, Tianyu; University of Maryland at College Park College of Computer Mathematical and Natural Sciences, Chemistry and Biochemistry Leonard, Matt; University of Maryland at College Park, Tsyshevskiy, Roman ; University of Maryland at College Park, Materials Science and Engineering Mcentee, Monica; monica.l.mcentee.civ@mail.mil Karwacki, Christopher; US Army, Edgewood Chemical Biological Center Durke, Erin; Edgewood Chemical Biological Center Kuklja, Maija; University of Maryland at College Park, Mater.Sci.Eng.; National Science Foundation, Office of the Director Rodriguez, Efrain; University of Maryland, Department of Chemistry and Biochemistry

High Reactivity of Mesoporous CeO_2 to Dissociate Chemical Warfare Agent Sarin

Tianyu Li[a], Matthew Leonard[a#], Roman Tsyshevsky[b#], Monica McEntee[c], Christopher Karwacki[c], Erin M. Durke[c], Maija M. Kuklja[b], and Efrain E. Rodriguez[a]

[a] Department of Chemistry and Biochemistry, University of Maryland, College Park, Maryland 20742, United States

[b]Department of Materials Science and Engineering, University of Maryland, College Park, Maryland 20742, United States

[c]US Army Combat Capabilities Development Command Chemical Biological Center, 8198 Blackhawk Road, Aberdeen Proving Ground, Maryland 21010, United States

#Both authors equally contribute to this study

Corresponding authors:

Maija M. Kuklja: mkukla@nsf.gov

Efrain E. Rodriguez: efrain@umd.edu

Keywords: Chemical warfare agents, mesoporous ceria, DFT modeling, quantum chemical calculations, decomposition reaction mechanisms, heterogenous surface reactions

Abstract

We perform spectroscopic surface characterization on mesoporous ceria (CeO_2) under exposure of Sarin gas, also known as GB. We find mesoporous CeO_2 displays extraordinary reactivity towards GB dissociation under high vacuum. The spectroscopic results combined with density functional theory (DFT) calculations suggest that the cleavage of the P-F and P-OR bonds are both possible pathways for GB to dissociate on the CeO_2 surfaces. The modeling reveals differences in dissociation pathways of GB on the crystallographic (111)- and (110)-surfaces of ceria. We also report some dissociation of GB on mesoporous CeO_2 under ambient conditions. The finding that mesoporous CeO_2 can degrade GB under mild conditions is encouraging and implies the strong potential of ceria-based materials to be applied in combating chemical warfare agents related to the GB series.

1. Introduction

The search for materials to effectively filter and decompose chemical warfare agents (CWAs) is in urgent need due to the continuing concern of such lethal chemical attacks in both global conflicts and terrorist attacks on civilian populations. One of the most notorious CWAs is Sarin gas, also known as GB (or gas B of the G-series). GB functions as a nerve agent and can cause instant lethal suffocation even under very low concentrations of exposure (~50-100mg/min/m^3)[1,2]. Several categories of materials have been studied to defeat GB and its simulant molecules including carbon-based materials[3–8] , metal-organic frameworks (MOFs)[9–15], polymer fibers [16–19], metal oxides[20–38] and their composites[39–42]. Metal oxides have several advantages over some of these categories due to their active and diverse surfaces. In addition, recent efforts to fashion metal oxides into mesoporous structures can effectively increase their surface areas to bolster their filtering propertiess[43,44].

Ceria (CeO_2) is a popular metal oxide that has been widely researched in the fields of catalysis and fuel cells due to the high activity on its surfaces and bulk lattice atoms[32,45–48]. CeO_2 has also attracted attention for combating CWAs recently, and it was proposed that it might display great activity towards GB decomposition; several recent experimental and computational studies demonstrate that CeO_2 can effectively dissociate a variety of GB simulant molecules at room temperature[25,29,49–53]. Our recent spectroscopic measurements and DFT calculations also indicate that CeO_2 surfaces are highly reactive toward degradation of dimethylmethylphosphonate (DMMP), which is a GB simulant[54]. Although these simulant molecules have some structural similarity to GB, the different chemical activity of the P-F bond and the larger P-OR group in GB might cause a significant difference in its interaction with metal oxide surfaces.

While there are several past studies of GB simulants interactions on CeO_2 [25,29,49,50,53], limited research has been performed to understand how exactly CeO_2 interacts with actual GB agent. Due to the

extreme toxicity of GB, it is not possible for most of laboratories to run GB-based experiments. However, such an experiment is necessary to examine the true potential of the proposed materials to combat GB. In addition, an experimental comparison between GB and its simulants can also elucidate whether such simulant molecules truly resemble GB in their reactivity with filter materials. Thus, for this study we performed a comprehensive surface characterization of dry mesoporous CeO_2 under exposure to GB and advanced DFT-based modeling of decomposition channels of GB on CeO_2.

Our observations for CeO_2 breaking down GB are encouraging. We find that the as-synthesized mesoporous CeO_2 displays extraordinary activity on GB dissociation at room temperature. Such a reaction occurs under vacuum and without any assistance from moisture or photo excitation. DFT calculations were performed to understand the origin of the high reactivity of CeO_2. Our modelling shows a relatively low activation energy barrier for GB to dissociate on the CeO_2. With the combination of spectroscopic measurement and DFT calculations, we also reveal possible reaction pathways. To our knowledge, this work is the first comprehensive report to actually explore and verify the reactivity of CeO_2 on GB dissociation. Our comprehensive surface characterization and DFT-based modeling suggests a strong potential of CeO_2 to be applied in combating CWAs.

2. Experimental Section

2.1 Synthesis of Templated Mesoporous CeO_2

Mesoporous CeO_2 was synthesized *via* a nanocasting method similar to the previously reported approach[55,56] . The silica template KIT-6 was first prepared from a reported method[57], for which 85 °C was used as the aging temperature during the KIT-6 synthesis. In our typical synthesis of mesoporous CeO_2, 0.5000 g of as-prepared KIT-6 silica was initially dispersed in 20.0 mL of 95% ethanol. Then, 1.362 g of $Ce(NO_3)_3{\cdot}6H_2O$ were dissolved in the same solution. The mixture was stirred at room temperature until all solvents evaporated and the mixture became a dry powder. The powder was later transferred into a glass vial (diameter ~ 5 mm) and calcined at 560 °C for 6 h (ramp rate = 1°C/min). During the calcination step $Ce(NO_3)_3{\cdot}6H_2O$ decompose and oxidizes

to pure CeO_2. To fully remove the silica template, the CeO_2/KIT-6 composite was soaked in a 2M NaOH solution at 80 °C overnight; this step was repeated three times. After washing 3 times with distilled water and twice with ethanol, the final mesoporous CeO_2 product was dried in air at 80°C overnight and then at 150°C for an additional 24 h.

2.2 Surface and Structural Characterization of Mesoporous CeO_2

Transmission electron microscopy (TEM) image was taken using a JEOL JEM 2100 LaB6 TEM system. Powder X-ray diffraction (XRD) pattern was recorded on the Bruker D8 Advance diffractometer with Cu Kα/Kb radiation. Rietveld refinements with the XRD patterns were performed using TOPAS 5[58]. The nitrogen adsorption isotherms were measured with a Micromeritics ASAP 2020 Porosimeter Test Station, and the surface area was calculated by applying the Brunauer−Emmett−Teller (BET) equation on adsorption data obtained at P/P_0 between 0.05 and 0.35. The pore size distributions were calculated by analyzing the adsorption branch of the N_2 sorption isotherm using the Barret−Joyner−Halenda (BJH) method. Ce 3d spectra were collected on a Kratos Axis 165 X-ray photoelectron spectrometer (XPS) operating in hybrid mode using Al Kα monochromatic X-rays at 280 W. All XPS spectra were calibrated to the C 1s peak at 284.80 eV, and fits were performed using CasaXPS. Shirley background was used for background subtraction, and the peaks fit with a 30% Gaussian+70% Lorentzian peak shape profile.

Carbon monoxide (CO) adsorption studies on CeO_2 were performed in a high vacuum chamber with a base pressure at $3x10^{-9}$ Torr. A more detailed description of the vacuum chamber is provided elsewhere[15]. The CeO_2 was pressed into a 0.004” thick W-grid and attached to the sample mount via stainless steel clamps connected to copper rods. The copper rods were attached to a power supply allowing for resistive heating of the sample up to ~1000 K at a resolution of ±0.1 K. Before introducing CO into the vacuum chamber, the sample was heated to 450 K for 30 minutes in order to remove H_2O and hydrocarbon impurities. After heating, the

surface was cooled down with liquid N_2 (~140 K) and an infrared (IR) spectrum was taken of the CeO_2 sample. An IR spectrum was taken of the W-grid without any CeO_2 powder and used as the background. Each IR spectrum contains an average of 256 interferograms at a resolution of 2 cm^{-1}. Subsequently, 10^{-2} Torr of CO vapor was introduced into the vacuum chamber. An IR spectrum of the sample was taken and was subtracted from the IR spectrum of CeO_2 prior to CO exposure. The subtracted spectrum represents a difference spectrum showing the CO adsorption on the CeO_2 surface.

2.2 IR Characterization of GB interaction with dry mesoporous CeO_2 under high vacuum

(**CAUTION!** Experiments performed with ultra-toxic CWAs require highly trained operators, extreme safety protocol and approved facilities.) Chemical Agent Standard Analytical Reference (CASARM)-grade sarin (95+% by NMR) was used for all experiments. Prior to dosing, the GB was purified through a freeze-pump-thaw cycle.

Spectroscopic (IR) measurements of mesoporous CeO_2 interacting with GB were performed in an ultra-high vacuum chamber with a base pressure of 9.3 x 10^{-9} Torr. The mesoporous CeO_2 was pressed into a 0.004” thick tungsten grid and attached to the sample mount with stainless steel clamps connected to copper rods. An IR spectrum was taken of the W grid without CeO_2 at each step and used to subtract any background interactions. Before the experiments, the sample was placed in vacuum for 24 h and then heated to 300 C° in the presence of O_2 for 1.5 h to remove any environmental gases (i.e., H_2O, carbonates, CO_2, NO_x, ect.). Subsequently, 10^{-4} Torr of GB vapor was introduced into the vacuum chamber to interact with the mesoporous CeO_2 sample. IR scans of the sample were taken every couple of minutes for a total of 60 min. After the experiment, the chamber with the sample was placed under vacuum for 10 days to examine how strong the GB is adsorbed on the surfaces of mesoporous CeO_2. The IR spectrum was also collected after the evacuation. Each IR spectrum includes 256 interferograms at a resolution of 2 cm^{-1}. After final dosing, the sample was evacuated and returned to a pressure of 10^{-9} Torr to determine what

remained on the surface. The scan prior to GB exposure was used as a background to create a difference spectrum.

2.3 Ambient diffuse reflectance infrared Fourier transform spectroscopy (DRIFTS)

(**CAUTION!** Ultra-toxic CWAs were used in the experiment. Such an experiment requires extreme care, highly trained staff, and a secure government-regulated facility.) The activity of mesoporous CeO_2 for GB degradation under ambient conditions was characterized in an in-situ environmental DRIFTS reaction cell maintained at 25 °C. A 6 mm porous ceramic cup was used as a sample holder. Approximately 20 mg of the sample was used.

A detailed DRIFTS instrument set-up is described elsewhere[59]. Helium gas (Airgas, 99.999% purity) was used to carry GB vapor. The carrier gas was first flown (10 mL/min) through a microsaturator cell containing a liquid reservoir of GB (maintained at 20 °C) before entering the sample cell. The GB flow was maintained for 90 min while DRIFTS IR spectra were recorded in-situ with a Thermo Fisher Scientific 6700 FTIR spectrometer. A background scan was collected prior to beginning the dosing experiment. During the dose, collected spectra were averaged over ~2 min with a 2 cm^{-1} resolution.

2.4 DFT Modeling of GB interacting with pristine CeO_2 surfaces

Solid state periodic calculations were performed with DFT[60,61] using the GGA PBE[62] functional and projector augmented-wave (PAW) pseudo-potentials[63], as implemented in the VASP code[64–66]. Hubbard's parameter U[67] was introduced to account for Ce 4f orbitals and was set to 4.0 eV in accordance with reported literature[68]. Grimme's D2[69] corrections were added to account for weak van der Waals interactions. Several previous theoretical studies[70–74] showed that an addition of Grimme's D2 correction to the DFT functional considerably improves a description of dispersion effects in the systems with weak non-covalent interactions. In simulating ideal bulk crystals (**Figure S1a**), atomic coordinates and lattice constants were allowed to relax simultaneously

without any symmetry constraints. The convergence criterion for electronic steps was set to 10^{-5} eV, and the maximum force acting on any atom was set not to exceed 0.01 eV/Å. Kinetic energy cut-off was set to 520 eV. In modeling the CeO_2 crystal, an 8×8×8 Monkhorst−Pack *k*-point mesh was used. The calculated lattice parameters of the CeO_2 cubic unit cell (**Figure S1a**) with $Fm\bar{3}m$ space group, *a*=5.37 Å, agree with the experimental lattice vectors (*a*= 5.41 Å[54] within ~1 %).

Our calculations of GB adsorption and decomposition were limited to modeling reactions on the most stable surfaces, including the (110)- and (111)-surfaces[54] (**Figure S1 b and c**), observed in our experiments. The model slab of the (110)-surface contained 252 atoms with the supercell lattice vectors of *a* = 16.23 Å, *b* = 14.92 Å, and *c* =31.61 Å. The model slab of the (111)-surface contained 240 atoms with the supercell lattice vectors of *a* = *b* = 15.03 Å, and *c* = 34.37 Å. A vacuum layer of 20 Å placed on top of the CeO_2 surfaces served to minimize interactions between the supercells in the z-direction and to avoid any significant overlap between the wave functions of periodically translated cells. All surface calculations were performed at G-point only. Kinetic energy cut-offs in modeling CeO_2 (110) and (111) surfaces were set to 520 eV. The convergence criterion for electronic steps was set to 10^{-5} eV, and the maximum force acting on any atom was set not to exceed 0.03 eV/Å.

Minimal energy paths in the VASP periodic calculations were obtained with the standard nudged elastic band method[75] . Atomic positions were relaxed using conjugate gradient and quasi-Newtonian methods within a force tolerance of 0.05 Å/eV. The convergence criterion for electronic steps was set to 10^{-5} eV.

3. Experimental Results

3.1 Material Characterizations

The samples used in this study are from the same batch of mesoporous CeO_2 that we previously used for a DMMP study[29]. The as-synthesized mesoporous CeO_2 is presented in **Figure 1**. An ordered mesoporous structure is visible from the TEM image (**Figure 1a**). Nitrogen adsorption isotherms and the corresponding pore size distribution curve (inset) are displayed in **Figure 1b**. The extracted BET surface area is 130.4 m^2/g, and the mean pore size is approximately 3.6 nm. The XRD pattern (**Figure 1d**) confirms that the samples are phase-pure, consisting of only cubic

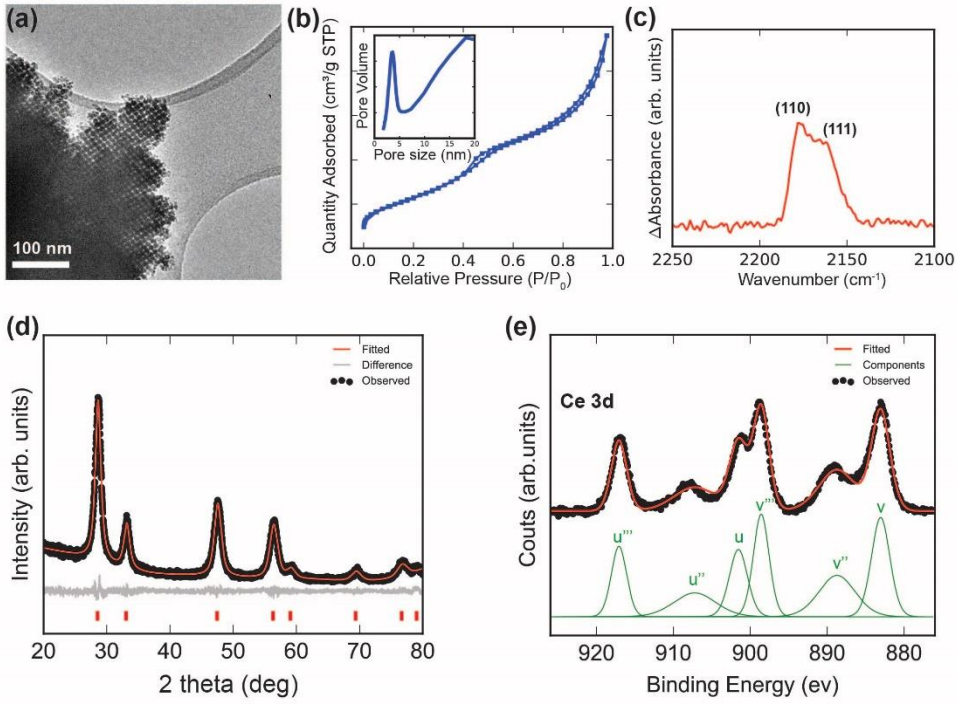

Figure 1. Structural and surface characteristics of as-synthesized mesoporous CeO_2: a) The TEM image confirm its KIT-6 mesoporous structure. b) The nitrogen adsorption isotherm and the resulting pore size distribution (inset) show an average pore size less than 5 nm. c) The IR spectrum of CO stretching modes when CO is adsorbed onto mesoporous CeO_2. reveal two peaks associated with the two surfaces, (110) and (111). d) The XRD pattern and subsequent Rietveld fit to it demonstrate phase purity. e) The Ce 3d XPS spectra and subsequent fitting reveal the predominant valence states. Reproduced with permission of the American Chemical Society[29].

CeO_2 with the fluorite-type structure (space group $Fm\bar{3}m$). The severely broadened diffraction peaks in the XRD pattern indicate a nanocrystalline nature of the mesoporous CeO_2. Ce 3d XPS is displayed in **Figure 1e**. The spectra can be well fit by applying only Ce^{4+} components[76], which implies that Ce^{4+} predominates as the Ce species on the surface. The IR absorption spectrum on CO stretching modes when CO is adsorbed on the mesoporous CeO_2 (**Figure 1c**) displays two major peaks at 2178 cm^{-1} and 2159 cm^{-1}, implying two major CeO_2 surfaces are exposed in

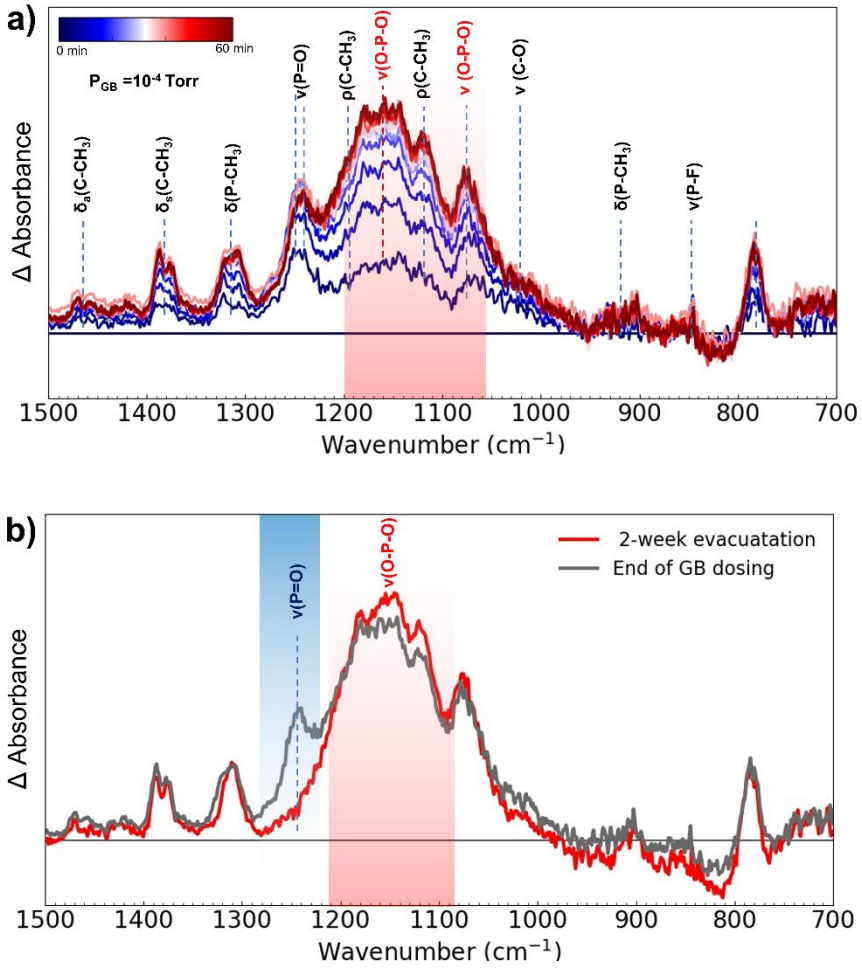

Figure 2. a) In situ difference IR spectrum of the surfaces of mesoporous CeO_2 upon GB exposure in the high vacuum. b) IR spectra of surfaces of mesoporous CeO_2 after GB exposure and after 2-week evacuation following the GB exposure.

mesoporous CeO_2. 2178 cm^{-1} corresponds to CO adsorbed on (110)-,and 2159 cm^{-1} to the (111)-surface.[77,78]

3.2 High reactivity of Mesoporous CeO_2 under high vacuum conditions

High vacuum experiments with live GB agent were performed on the as synthesized mesoporous CeO_2 at room temperature. The sample was placed in high-vacuum for 24h and then heated in the presence of oxygen to obtain a relatively hydroxylation-free and oxygen vacancy-free surfaces before the experiments. The GB gas was then introduced into the high vacuum chamber for 60 min at a constant pressure of 10^{-4} Torr.

Figure 2a displays the in-situ difference IR spectrum of the surfaces of mesoporous CeO_2 during the GB exposure (scans taken every 5 minutes). The major peaks are assigned accordingly in **Figure 2** and listed in **Table 1**. We are unsure about the assignment of the mode at 780 cm^{-1} as limited literatures discussed this mode. In a report on the IR spectra of Organophosphorus Compounds, this mode was assigned as w(POC)[79]. The vibrational modes of δ_a (C-CH_3), δ_s (C-CH_3), δ(P-CH_3), ν(P=O), ν_a (C-O), ν_s (C-O) and ν(P-F) exist in the structure of intact GB[80]. The gradual increase of these bands upon initial GB dosing indicates that intact GB molecules are

Table 1. IR Frequencies (cm^{-1}) of GB in the Vapor Phase, GB Adsorbed on CeO_2 characterized by vacuum IR and ambient DRIFTS.

GB vapor (cm^{-1})	GB adsorbed on CeO2 (cm^{-1}) (high vacuum IR)	GB flow through CeO_2 (cm^{-1}) (DRIFTS)	IR band assignments
1468	1460, 1470	\	$\delta_{as}(CH_3C)$
1380	1375, 1388	1370, 1380	$\delta_s(CH_3C)$
1328	1310, 1320	1322	δ(P–CH_3)
1303	1240, 1245	1245, 1277	ν(P=O)
1183/1111	1190/1120	1190/1120	ρ(CH_3C)
\	1100–1200	1100–1200	ν(O–P–O)
\	1080	\	ν(O–P–O)
1020	1020-1030	1030	ν(C–O)
928	920	\	δ(P–CH_3)
845	845	\	ν(P–F)

readily adsorbed onto the surfaces of mesoporous CeO_2. The vibration bands of intact GB molecule stop growing after 20 minutes as the GB adsorption reaches saturation on CeO_2. The missing signature bands from OH group (3100 – 3800cm^{-1} shown in **Figure S2**, and ~1500 cm^{-1}) in the difference spectrum imply that GB is interacting with the dry surfaces of mesoporous CeO_2.

The dissociation of the GB molecule is also evident in the IR spectrum in addition to its intact form. A very broad band containing several peaks between 1100-1200 cm^{-1} also grow upon GB dosing. This region signifies the stretching vibration of the O-P-O groups and is generally regarded as a strong indication of GB decomposition[23,24,33,59,81,82]. We realize ρ(C-CH_3) modes from intact GB molecules also appear in this region (~1180 cm^{-1} and 1120 cm^{-1}); however, the intensity of ρ(C-CH_3) is relatively weak in the IR spectrum according to previous studies[23,24,33,59,81,82] on DMMP and GB molecules. Therefore, ρ(C-CH_3) modes are not a major contribution for the growing intensity of this region, and we are confident that O-P-O groups form on the surfaces of CeO_2.

The very broad and multi-peak nature of ν(O-P-O) in the spectrum indicates there might be multiple O-P-O configurations on the surfaces of mesoporous CeO_2. Since the as-synthesized mesoporous CeO_2 has both the (110) and (111) surfaces exposed, it is possible GB decomposition on the two different surfaces leads to disparate O-P-O configurations. In addition, GB can either lose F or -$OCH(CH_3)_2$ to form various O-P-O configurations on the surface, or even lose both F and -$OCH(CH_3)_2$ to form $RP(-O)_3$ with three P-O bonds, as presented in **Scheme 1**. Even though we are not clear which O-P-O configuration(s) contribute to the broad band, there is no doubt they all come from the degradation of GB.

The dissociation of GB molecules is also evidenced by the splitting bands of δ(P-CH_3). As shown in **Figure 2a,** doublets separated by ~10 cm^{-1} are all visible for δ(P-CH_3) modes. It is reported that

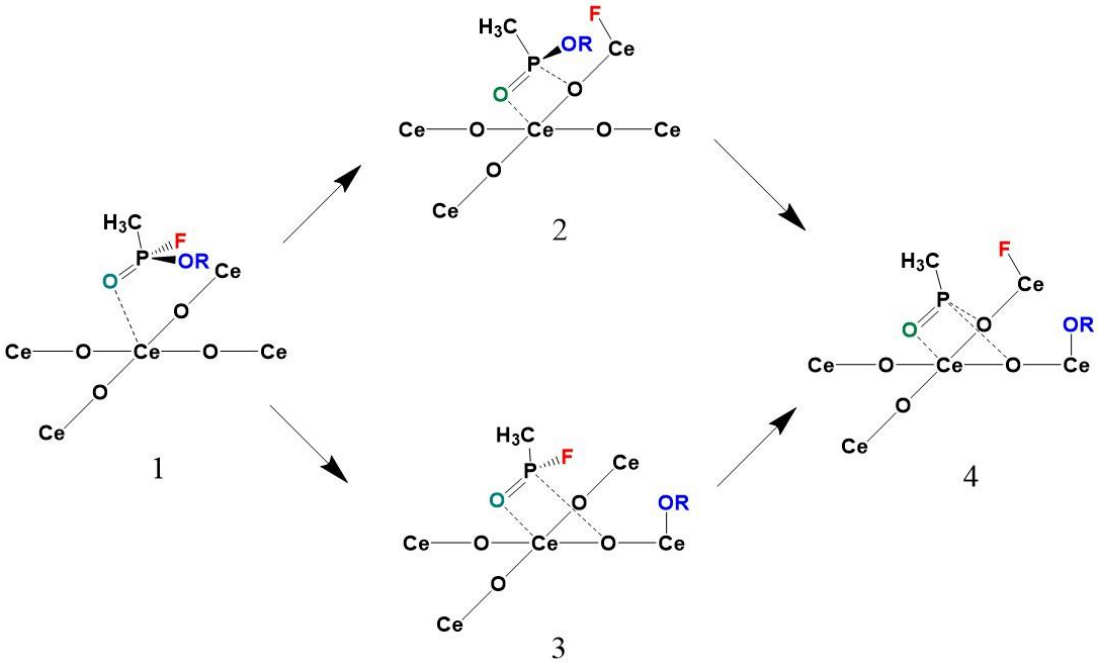

Scheme 1. Possible pathways for Sarin (GB) decomposing on the CeO_2 surface, which leads to various O-P-O configurations experimentally observed in the IR spectra.

cleavage of the P-F bond or the leaving of -$OCH(CH_3)_2$ group from GB molecules can lead to the redshift of this bending mode[24,59,81,82].

After the final GB exposure, the sample was evacuated under the base pressure of $7x10^{-9}$ torr for 2 weeks. The sample was re-scanned with IR and the comparison with the final scan under GB exposures is presented in **Figure 2b**. Most notably, the v(P=O) mode at 1240 cm^{-1}, completely disappeared. While the bands (1100-1200 cm^{-1}) associated with v(O-P-O) increased significantly. This means that the adsorbed GB molecules continued to dissociate on the surfaces of CeO_2, leading to the breaking of P=O bonds to form the O-P-O species. We also observed the intensities of other major bands in the spectrum remain nearly unchanged after two weeks under ultra-high vacuum, implying strong non-reversible adsorption of the decomposition species from GB on the surfaces of mesoporous CeO_2.

3.3 Mesoporous CeO_2 interacting with GB under ambient conditions.

The activity of mesoporous CeO_2 towards GB under ambient condition is also explored via diffuse reflectance infrared Fourier transform spectroscopy (DRIFTS). The flow line set-up in DRIFTS cannot fully eliminate moisture both in the gas flow and samples. Therefore, in contrast with the high vacuum IR experiment mentioned previously, the mesoporous CeO_2 tested in DRIFTS is more or less hydroxylated, which better resembles the practical conditions when materials are put into applications. **Figure 3** displays the difference DRIFTS spectra of the surface of mesoporous CeO_2 under flow of GB vapor for 6 min (**Figure 3a**) and 90 min (**Figure 3b).** Most IR bands appearing here resemble what we have observed in the vacuum IR experiment (**Figure 2**) and can be assigned based on **Table 1.**

A notable difference is that a shoulder peak at 1277 cm^{-1} is observed in the DRIFTS spectra but not in the high vacuum IR spectra. This peak most likely belongs to v(P=O) mode of the GB when

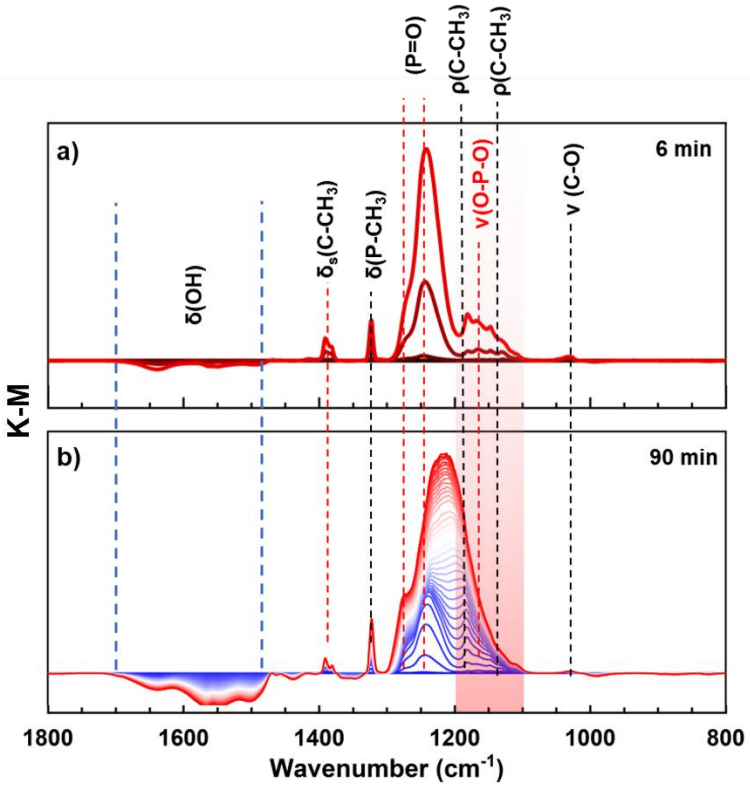

Figure 3. DRIFTS measurement spectrometry of mesoporous CeO_2 upon GB dosing under ambient conditions with He flow.

GB is adsorbed on the surface through the hydrogen bond interaction with surface hydroxyl groups[23,28,59]. The v(P=O) mode when GB interacts with pristine CeO_2 surfaces is observed at ~1230 cm^{-1}. We made such an attribution because v(P=O) mode at 1230 cm^{-1} appears also at the high vacuum IR experiment (**Figure 2**). The two distinct v(P=O) modes observed in the DRIFTS measurement indicate that the mesoporous CeO_2 possesses both hydroxylated regions and pristine (dry) regions on the surfaces. Compared with the v(P=O) mode when GB interacts with pristine surface, a significant blueshift (~40 cm^{-1}) is observed for the v(P=O) mode when GB interacts with surface hydroxyl groups, implying a weaker adsorption strength of GB on hydroxylated surfaces than on pristine surfaces. The weaker adsorption strength of GB on hydroxylated surfaces can be attributed to the various dominant interactions between pristine and hydroxylated surfaces. Pristine CeO_2 surfaces have under-coordinated Ce atoms exposed, which can provide empty *f*-orbitals for lone pairs electrons of P=O to coordinate, forming relatively stronger covalent interactions. While on the hydroxylated surfaces, hydroxyl group (-OH) rather than under-coordinated Ce atoms are exposed, so a hydrogen bond (P=O----HO), which is weaker than covalent interaction, dominates GB interactions with the surface. The interaction between hydroxylated surfaces and GB are also evident by the gradual decrease of δ (OH) bands between 1500~1700 cm^{-1}. The decrease of δ (OH) bands implies the surface OH or H_2O was consumed through hydrogen bond formation or being replaced by adsorbed GB molecules. The very broad nature of δ (OH) bands implies there are different configurations of OH groups available on the surfaces.

Similar as in the high vacuum IR spectra (**Figure 2**), the rise of v(O-P-O) bands at 1100-1200 cm^{-1} is observed in the DRIFTS measurement (**Figure 3**), an indication of the GB degradation. However, unlike the high vacuum IR spectra, the relative intensities of v(O-P-O) are never comparable to v(P=O) throughout the whole GB flow period. We conclude the activity of the

mesoporous CeO_2 is more reactive in the high vacuum environment than under ambient conditions.

As GB flow continues, most of the IR modes from intact GB molecules continue growing while the v(O-P-O) becomes less obvious in the spectra, as shown in **Figure 3b.** The plateau of the v(O-P-O) modes in the DRIFTS spectra implies that the active sites of CeO_2 surfaces for GB degradation are saturated and cannot be spontaneously regenerated or reused. Therefore, the degradation of GB on the surfaces of CeO_2 is better described as being a heterogeneous surface-molecule reaction rather than a catalytic reaction. In other words, the surfaces of CeO_2 behave more as a reactant instead of a catalyst when decomposing GB.

3.4 Understanding the high activity of CeO_2 via DFT Modeling

Both high vacuum IR measurements and ambient DRIFTS measurements show that GB can actively dissociate on the mesoporous CeO_2. The measurements imply the high reactivity mainly comes from the dry pristine surfaces as the CeO_2 shows decreased activity under ambient conditions with hydroxylated surfaces. Here, we performed DFT modeling to understand the high activity of pristine surfaces of mesoporous CeO_2 towards GB dissociation. The CO adsorption IR characterization of CeO_2 mesoporous materials (**Figure 1c**) indicates that the as-synthesized mesoporous CeO_2 possesses both (110) and (111) surfaces. Thus, we modeled the GB adsorption and decomposition on the (110) and (111) CeO_2 surfaces to obtain better understanding of GB interactions with mesoporous ceria and provide a consistent interpretation of our experimental observations. In this work, we focus on the interactions of GB with pristine dry CeO_2 surfaces.

GB Adsorption on (110) and (111) CeO_2 Surfaces.

GB is strongly adsorbed on pristine (110) and (111) surfaces through its phosphoryl oxygen (**Figure 4 a-f**). For CeO_2 (101) surface, the obtained adsorption energy varies from 136 to 171.5

kJ mol^{-1}. Adsorption on CeO_2 (111) is weaker than on the (110) surface with the adsorption energy 124-147.5 kJ mol^{-1}. This is consistent with the trends we earlier observed for DMMP adsorption on CeO_2 (110) and (111) surfaces[29]. **Figure 4** indicates a relatively large contribution of hydrogen bonding in energies of GB adsorption on CeO_2. Thus, configurations M2 and M4 have adsorption energies of -135.9 kJ mol^{-1} and -133.5 kJ mol^{-1}, respectively, and correspond to the structures with the least favorable adsorption energies on the (110) and (111) surfaces, respectively. In configuration M2, GB forms a hydrogen bond with lattice oxygens through one of its hydrogen atoms. In the configuration M4, the molecule is orientated on the (111) surface in such a way that no hydrogen bonds can be formed. Contrastingly, in the configuration M3, GB forms hydrogen bonds with the lattice oxygen on CeO_2 (110) surface through at least two of its hydrogens. As a result, the configuration M3 corresponds to the structure with the most favorable calculated adsorption energy of -171.5 kJ mol^{-1}. On the (111) surface, the configuration M6, in which GB forms a hydrogen bond with one of the lattice oxygens, corresponds to the structure with the highest adsorption energy of -147.5 kJ mol^{-1}. We have noted an effect of hydrogen bonding on GB adsorption on metal oxides, including ZnO[83], MoO_2[84] and TiO_2[24]. Based on energetic considerations, CeO_2, particularly, its (110) surface, demonstrates stronger adsorption than ZnO (10-10) surface (-171.5 for CeO_2 vs -133 kJ mol^{-1} for ZnO) [83], TiO_2 anatase (101) surface (-171.5 vs -129 kJ mol^{-1}) [24], and CuO (111) surface (-171.5 vs -139.2 kJ mol^{-1})[85]. The energy of GB adsorption on rutile (110) surface (-171 kJ mol^{-1})[24] is close to GB adsorption on CeO_2 (111) surface. Considerably stronger adsorption was calculated for GB adsorption on the MoO_2 (011) surface (200-230 kJ mol^{-1})[84]. Comparison of calculated adsorption energies for different materials shows that CeO_2 demonstrates attractive properties overall for GB adsorption.

GB Decomposition on (110) and (111) CeO_2 Surfaces.

In studying GB decomposition on CeO_2 (110) and (111) surfaces, we modeled the three most plausible mechanisms: 1) the propene elimination, 2) the P-F bond scission, and 3) the P-OC_3H_7 bond scission (**Figure 5a and b**). An elimination of propene (A1-A2) on the (110) surface requires 81.1 kJ mol^{-1}. The reaction is highly exothermic and proceeds with the energy release of 130 kJ mol^{-1}. The propene elimination on the (111) surface (B1-B2) requires a noticeably higher energy of 120 kJ mol^{-1}. In addition, the mechanism has a reaction energy of only -3.6 kJ mol^{-1}. Our calculations show that elimination of propene on CeO_2 (110) surface is an energetically favorable reaction as it requires considerably lower activation energy than on CeO_2 (111) and other metal

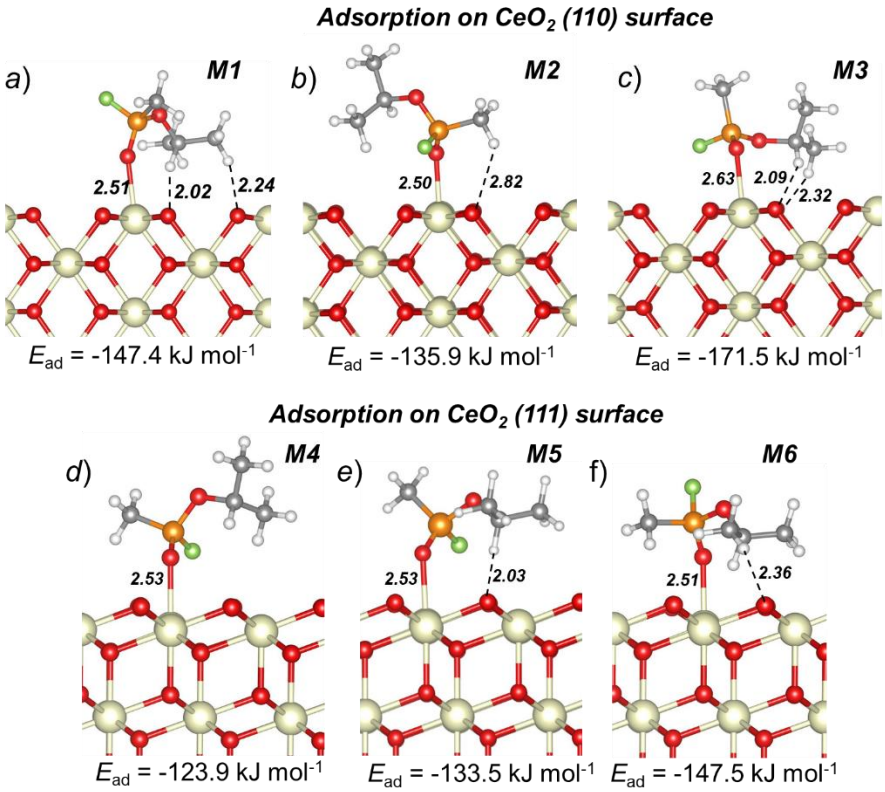

Figure 4. Adsorption of GB molecule on CeO2 (a)-(c) (110) and (d)-(f) (111) surfaces. Bond distances are in Angstroms. (Ce atoms are in gold color, oxygen – red, phosphorus – orange, fluorine – green, carbon – grey, hydrogen - white).

oxides including the surfaces of the following: CuO (111) 111.9 kJ mol^{-1} [85], ZnO (10-10) 113 kJ mol^{-1}[83], TiO_2 anatase (101) 122.6 kJ mol^{-1} [24] and TiO_2 rutile (110) 108 kJ mol^{-1}. [24]

Decomposition of GB on the CeO_2 (110) surface via the P-F bond scission (path A1-A3) requires 59.3 kJ mol^{-1}. The reaction is exothermic with calculated reaction energy of -91.9 kJ mol^{-1}. Breaking of P-F bond on (111) surface (path B1-B3) requires 69.2 kJ mol^{-1}, which is 10 kJ mol^{-1} higher than the same reaction on CeO_2 (110) surface. Similar to the (110) surface, the reaction on the (111) surface is an exothermic process although the reaction energy of GB degradation on (111) surface via P-F bond is 54.2 10 kJ mol^{-1} lower than that on (110) surface (-37.7 kJ mol^{-1} vs -91.9 kJ mol^{-1}). A comparison of the calculated activation energies of the surface facilitated P-F bond cleavage with the activation energies reported for other oxide materials shows that decomposition of GB on CeO_2 (110) and (111) surfaces requires considerably lower energies than on other metal oxides. Thus, decomposition of GB via the P-F bond cleavage on ZnO (10-10) requires 113.6 kJ mol^{-1} [83], TiO_2 anatase (101) – 142.8 kJ mol^{-1} [24], TiO_2 rutile (110) – 191.3 kJ mol^{-1} [24], CuO (111) – 106.3 kJ mol^{-1} [85], and MoO_2 (111)– 106.3 kJ mol^{-1} [84].

The decomposition of GB on CeO_2 (110) surface via the scission of the P-OC_3H_7 bond (path A1-A4) requires 44.8 kJ mol^{-1}, which is the lowest activation energy among three channels simulated in this work. Therefore, this pathway should dominate GB decomposition on the (110) surface. In addition to the low activation barrier, the surface facilitated breaking of the P-OC_3H_7 bond (path A1-A4) is a thermodynamically favorable process with the calculated reaction energy of -103.1 kJ mol^{-1}. Decomposition of GB on CeO_2 (111) surface via the P-OC_3H_7 bond scission requires a significantly lower energy than on other metal oxides including CuO (111) – 153.4 kJ mol^{-1} [85], ZnO

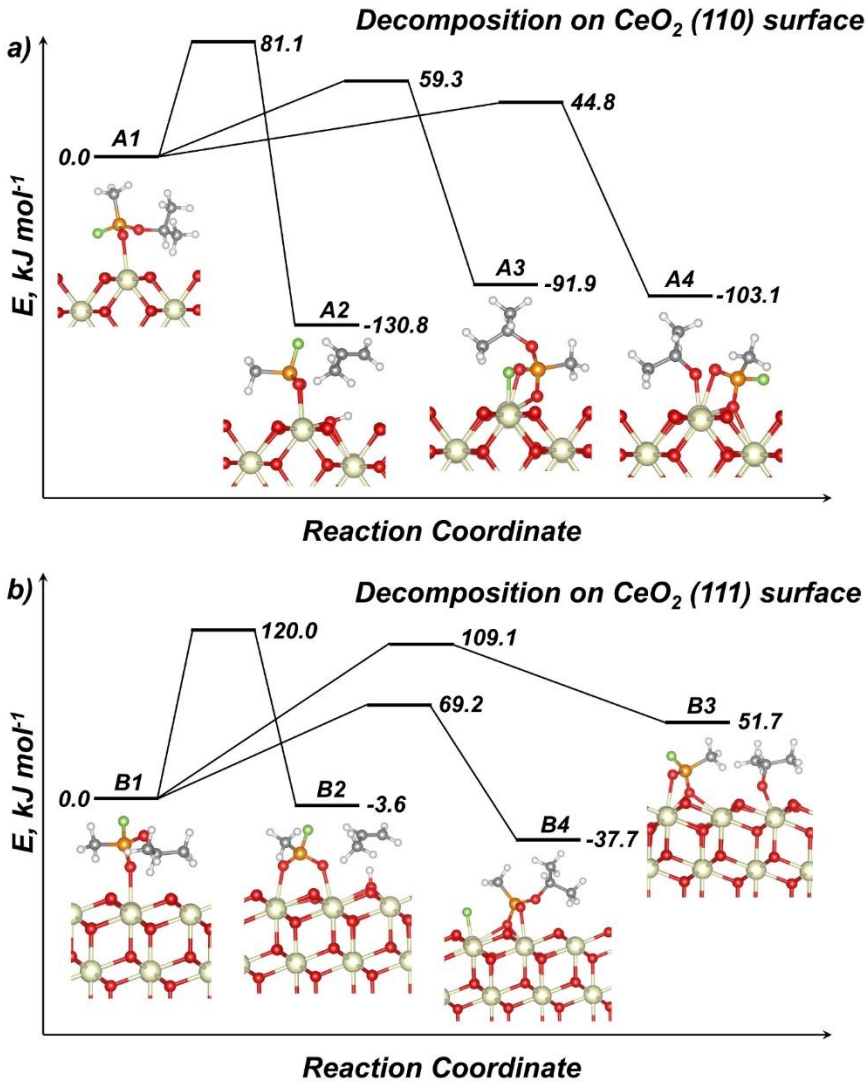

Figure 5. GB decomposition on CeO_2 a) (110) and b) (111) surfaces. (Ce atoms are in gold color, oxygen – red, phosphorus – orange, fluorine – green, carbon – grey, hydrogen - white).

(10-10) - 114.9 kJ mol^{-1} [83], TiO_2 rutile (110) – 212.9 kJ mol^{-1} [24], and MoO_2 (111)– 178.4 kJ mol^{-1} [84]. Decomposition of GB on the (111) surface via the P-OC_3H_7 bond cleavage (path B1-B4) requires 109.1 kJ mol^{-1}, which is 55 kJ mol^{-1} higher than the activation barrier of the P-OC_3H_7 bond cleavage on (110) surface (A1-A4, 44.8 kJ mol^{-1}). Furthermore, the reaction of P-OC_3H_7 bond cleavage on the (111) surface (path B1-B4) is an endothermic process with calculated reaction energy of 51.7 kJ mol^{-1}.

The propene elimination has the highest activation barriers on the (110) and (111) surfaces (81 and 120 kJ mol^{-1}) (among probed reaction mechanisms) and, therefore, unlikely competes with the decomposition channels involving the P-OC_3H_7 and P-F bond scission at room temperature.

4. Discussion

In agreement with the reported high reactivity of CeO_2 materials to dissociate the nerve agent simulants[25,29,49,50,53], the high activity of mesoporous CeO_2 to degrade the real nerve agent GB was verified in this study. Our high vacuum IR measurements show that GB molecules effectively adsorb onto the mesoporous CeO_2 and react with the surfaces at room temperature without any assistance of moisture or photo excitement. The dissociation of GB on the CeO_2 surfaces is found to be surface reaction rather than catalytic reaction, meaning that the surfaces behave as reactants upon GB degradation. A filter material must be able to quickly and irreversibly adsorb or absorb GB in order to be effective. In this regard, as a reactant, CeO_2 can interact with sarin in a chemical manner, potentially leading to rapid and irreversible adsorption of the GB. This property makes ceria a promising candidate for use as a filter material in protective equipment such as masks and protective clothing.

We believe that several key factors contribute to the high activity of CeO_2 towards GB dissociation. Firstly, the empty 4f/5d orbitals and large size of Ce^{4+} ions create a favorable environment for the coordination of P=O bonds in GB, effectively weakening the bonds of GB and promoting its

dissociation. Furthermore, the dissociation of GB on metal oxides typically results in the formation of O-P-O species on the surface (as shown in **Scheme 1**). The stability of these O-P-O species plays a crucial role in the activity of the surface(thermodynamically). The structure of CeO_2 is particularly well-suited to support their formation due to the Ce-O distance of approximately 2.3 Å, which matches the tetrahedral geometry of O-P-O species. This leads to relatively favorable decomposition of O-P-O on CeO_2. Similarly, both GB simulant DMMP and DMNP contain P=O in their structure and form O-P-O species upon dissociation. Therefore, both DMMP and GB are effectively dissociated on the surfaces of CeO_2[25,29,49–53].

Our DFT modeling further suggests feasible low-activation-energy pathways for GB to dissociate on both CeO_2 pristine (110) and (111) surfaces, which explains the high reactivity of CeO_2 observed in the experiment. Our modeling shows that GB can dissociate via the P-OC_3H_7 bond scission and P-F bond breaking, with dissociated species of GB greatly stabilized through binding with the surfaces. At the same time, our modeling demonstrates that GB dissociation via the P-OC_3H_7 bond scission and P-F bond breaking are not equally favored on (110) and (111) surfaces due to the different surface structures.

An analysis of the calculated data shows that GB decomposition via the P-OC_3H_7 bond scission will slightly dominate the overall GB decomposition on (110) surface, whereas the P-F bond scission will be the major decomposition channel on the (111) surface. The decomposition of GB via the P-OC_3H_7 bond scission on the (111) surface will likely be precluded due to the high activation energy (B1-B4, 100.9 kJ mol^{-1}) and endothermic nature of the reaction, as it is shown in **Figure 5b**. We suspect such a huge preference of the P-F bond scission over the P-OC_3H_7 bond scission is a result of the steric hindrance effect on the (111) surfaces. Compared with (110) surface, Ce atoms are embedded more deeply below the oxygen atoms on (111) surface (**Figure S1 b and c**). Thus, the (111) surface poses a stronger steric repulsion force coming from the top oxygen atoms when the species interact with the Ce atoms on the surfaces.

The P-F bond scission requires that the fluorine atom of the GB molecule be positioned close to undercoordinated Ce atoms, leading to attachment of the F atom onto Ce atoms. While P-OC_3H_7 bond scission requires -OC_3H_7 of the GB molecule positioned close to the undercoordinated Ce atoms, this proximity will lead to the attachment of -OC_3H_7 onto Ce atoms. The -OC_3H_7 is a much larger group than F thus will experience a larger steric repulsion force when it moves closer or is attached onto Ce atoms on (111) surfaces, which contributes to the rise of the activation energy and destabilizes the final dissociation products. In conclusion, P-OC_3H_7 bond breaking is slightly favored on CeO_2 (110) surface while P-F bond breaking is strongly favored on the (111) surface.

The active dissociation of GB on mesoporous CeO_2 is also observed under ambient conditions through DRIFTS while the activity is lower than in the high vacuum case. Since in the DRIFTS measurement GB is constantly flowing through the materials, a multilayer adsorption of GB on mesoporous CeO_2 is likely to occur. Once the first layer of GB dissociates, the surfaces of CeO_2 deactivate, so that other layers of GB remain intact, resulting in the “observed” lower activity. This again suggests the surfaces of CeO_2 behave like an active reactant rather than catalyst when interacting with GB. Another possible cause for the lower activity of CeO_2 under ambient conditions is that of hydroxylation of the surfaces, which reduces reactivity in comparison with the pristine surface. On surfaces that are exposed to moisture, it is possible for GB to undergo hydrolysis with surface water and hydroxylation. However, the activity of the hydrolysis of GB seems to be weaker than its dissociation on the pristine CeO_2 surfaces. Indeed, our previous modeling study showed that hydroxylated CeO_2 surfaces are less reactive than the pristine surfaces towards DMMP dissociation as hydroxyl groups can block active undercoordinated Ce sites for the stabilization of dissociated methoxy species[29]. Given the structural similarity between GB and DMMP (GB also contains alkoxy group), hydroxyl groups on the CeO_2 might prevent the GB to dissociate into stable species on the surfaces as well.

5. Conclusion

In summary, we experimentally demonstrated that mesoporous CeO_2 can strongly adsorb and actively decompose GB on its surfaces both in vacuum and under ambient conditions. Our DFT modeling suggests strong GB adsorption on surfaces of CeO_2 and reveals low-activation-energy pathways for GB to dissociate on both CeO_2 pristine (110) and (111) surfaces, which explains the high reactivity of CeO_2 observed in the spectroscopic measurements. Our study finds potential for CeO_2 to be incorporated in filter materials to combat nerve agents such as GB. Though our experiments and DFT modeling show exciting results on the high reactivity of CeO_2 materials towards GB decomposition, we admit that further studies under more realistic conditions could help better understand GB decomposition in mesoporous ceria. For example, the influence of the moisture (H_2O) should be systematically explored as water exist everywhere in the real world and different amount of water can show different degrees of impact on both sarin adsorption and dissociation. In addition, more realistic conditions would also admit for the presence of O_2, which was not considered in the current study. Future work should further explore the activity of CeO_2 materials under the an O_2 -containing atmosphere to validate their potential to combat nerve agents, as oxygen can interact with CeO_2[86] and might significantly interfere or indeed enhance the interaction between CeO_2 surfaces and GB molecules.

Acknowledgment

This work was funded by the Department of Defense (Grant HDTRA1-15-1-0005 and HDTRA1-19-1-0001). R.T. and M.M.K acknowledge support from NSF XSEDE (Grant DMR-130077) and DOE NERSC (Contract DE-AC02-05CH11231) resources, as well as computational resources at the Maryland Advanced Research Computing Center (MARCC) and University of Maryland supercomputing resources (http://hpcc.umd.edu). MMK is grateful to the Office of the Director of National Science Foundation for support under the Independent Research and Development program. Any appearance of findings, conclusions, or recommendations expressed in this material are those of the authors and do not necessarily reflect the views of NSF.

Conflict of Interest

Authors declare no conflicts of interests.

References

1 Institute of Medicine, *Gulf War and Health: Volume 1: Depleted Uranium, Sarin, Pyridostigmine Bromide, and Vaccines.*, National Academies Press (US), 2000.

2 S. J. Barr, *Top. Emerg. Med.*, 1985, **7**, 62–70.

3 S. S. Kiani, A. Farooq, M. Ahmad, N. Irfan, M. Nawaz and M. A. Irshad, *Environ. Sci. Pollut. Res.*, 2021, **28**, 60477–60494.

4 J. Claudot, E. Soubeyrand-Lenoir and G. Maurin, *Appl. Surf. Sci.*, 2021, **551**, 149433.

5 Q. Han, L. Yang, Q. Liang and M. Ding, *Carbon N. Y.*, 2017, **122**, 556–563.

6 N. K. Jaiswal and G. Kovačević, *Appl. Surf. Sci.*, 2019, **480**, 759–764.

7 J. Claudot, E. Soubeyrand-Lenoir and G. Maurin, *Appl. Surf. Sci.*, 2021, **538**, 148047.

8 H. Kaur, D. K. K. Randhawa, M. Khosla and R. K. Sarin, *Mater. Today Proc.*, 2020, **28**, 1985–1989.

9 I. Matito-Martos, P. Z. Moghadam, A. Li, V. Colombo, J. A. R. Navarro, S. Calero and D. Fairen-Jimenez, *Chem. Mater.*, 2018, **30**, 4571–4579.

10 M. C. De Koning, M. Van Grol and T. Breijaert, *Inorg. Chem.*, 2017, **56**, 11804–11809.

11 D. T. Lee, J. Zhao, G. W. Peterson and G. N. Parsons, *Chem. Mater.*, 2017, **29**, 4894–4903.

12 F. A. Son, M. C. Wasson, T. Islamoglu, Z. Chen, X. Gong, S. L. Hanna, J. Lyu, X. Wang, K. B. Idrees, J. J. Mahle, G. W. Peterson and O. K. Farha, *Chem. Mater.*, 2020, **32**,

4609–4617.

13 J. E. Mondloch, M. J. Katz, W. C. Isley, P. Ghosh, P. Liao, W. Bury, G. W. Wagner, M. G. Hall, J. B. Decoste, G. W. Peterson, R. Q. Snurr, C. J. Cramer, J. T. Hupp and O. K. Farha, *Nat. Mater. 2014 145*, 2015, **14**, 512–516.

14 M. R. Momeni and C. J. Cramer, *ACS Appl. Mater. Interfaces*, 2018, **10**, 18435–18439.

15 J. A. Harvey, M. L. McEntee, S. J. Garibay, E. M. Durke, J. B. DeCoste, J. A. Greathouse and D. F. Sava Gallis, *J. Phys. Chem. Lett.*, 2019, **10**, 5142–5147.

16 L. Ma, J. Xie, X. Yan, Z. Fan, H. Li, L. Lu, L. Chen, Y. Xin and P. Yin, *Chinese Chem. Lett.*, , DOI:10.1016/J.CCLET.2021.10.059.

17 D. Jung, P. Das, A. Atilgan, P. Li, J. T. Hupp, T. Islamoglu, J. A. Kalow and O. K. Farha, *Chem. Mater.*, 2020, **32**, 9299–9306.

18 D. M. Mizrahi, S. Saphier and I. Columbus, *J. Hazard. Mater.*, 2010, **179**, 495–499.

19 T. G. Grissom, A. M. Plonka, C. H. Sharp, A. M. Ebrahim, Y. Tian, D. L. Collins-Wildman, A. L. Kaledin, H. J. Siegal, D. Troya, C. L. Hill, A. I. Frenkel, D. G. Musaev, W. O. Gordon, C. J. Karwacki, M. B. Mitchell and J. R. Morris, *ACS Appl. Mater. Interfaces*, 2020, **12**, 14641–14661.

20 R. Yoo, S. Yoo, D. Lee, J. Kim, S. Cho and W. Lee, *Sensors Actuators B Chem.*, 2017, **240**, 1099–1105.

21 R. B. Balow, J. G. Lundin, G. C. Daniels, W. O. Gordon, M. McEntee, G. W. Peterson, J. H. Wynne and P. E. Pehrsson, *ACS Appl. Mater. Interfaces*, 2017, **9**, 39747–39757.

22 D. A. Panayotov and J. R. Morris, *J. Phys. Chem. C*, 2009, **113**, 15684–15691.

23 D. A. Panayotov and J. R. Morris, *Langmuir*, 2009, **25**, 3652–3658.

24 R. Tsyshevsky, M. McEntee, E. M. Durke, C. Karwacki and M. M. Kuklja, *ACS Appl. Mater. Interfaces*, 2021, **13**, 696–705.

25 I. Trenque, G. C. Magnano, J. Bárta, F. Chaput, M. A. Bolzinger, I. Pitault, S. Briançon, K. Masenelli-Varlot, M. Bugnet, C. Dujardin, V. Čuba and D. Amans, *CrystEngComm*, 2020, **22**, 1725–1737.

26 S. Jeon, I. V. Schweigert, P. E. Pehrsson and R. B. Balow, *ACS Appl. Mater. Interfaces*, 2020, **12**, 14662–14671.

27 S. Holdren, R. Tsyshevsky, K. Fears, J. Owrutsky, T. Wu, X. Wang, B. W. Eichhorn, M. M. Kuklja and M. R. Zachariah, *ACS Catal.*, 2018, **9**, 902–911.

28 Wesley O. Gordon, and Brian M. Tissue and J. R. Morris*, *J. Phys. Chem. C*, 2007, **111**, 3233–3240.

29 T. Li, R. Tsyshevsky, L. Algrim, M. McEntee, E. M. Durke, B. Eichhorn, C. Karwacki, M. R. Zachariah, M. M. Kuklja and E. E. Rodriguez, *ACS Appl. Mater. Interfaces*, 2021, **13**, 54597–54609.

30 S. Mukhopadhyay, M. Schoenitz and E. L. Dreizin, *Def. Technol.*, 2021, **17**, 1095–1114.

31 A. R. Head, R. Tsyshevsky, L. Trotochaud, Y. Yu, L. Kyhl, O. Karslloğlu, M. M. Kuklja, H. Bluhm, O. Karslıoğlu, M. M. Kuklja and H. Bluhm, *J. Phys. Chem. C*, 2016, **120**, 29077–29088.

32 T. Montini, M. Melchionna, M. Monai and P. Fornasiero, *Chem. Rev.*, 2016, 116, 5987–6041.

33 C. N. Rusu and J. T. Yates, *J. Phys. Chem. B*, 2000, **104**, 12292–12298.

34 T. M. Tesfai, V. N. Sheinker and M. B. Mitchell, *J. Phys. Chem. B*, 1998, **102**, 7299–7302.

35 S. R. Segal, L. Cao, S. L. Suib, X. Tang and S. Satyapal, *J. Catal.*, 2001, **198**, 66–76.

36 M. K. Templeton and W. H. Weinberg, *J. Am. Chem. Soc.*, 1985, **107**, 97–108.

37 Y. Xi. Li and K. J. Klabunde, *Langmuir*, 2002, **7**, 1388–1393.

38 M. B. Mitchell, V. N. Sheinker, A. B. Tesfamichael, E. N. Gatimu and M. Nunley, *J. Phys. Chem. B*, 2003, **107**, 580–586.

39 X. Zhang, Y. Sun, Y. Liu, Z. Zhai, S. Guo, L. Peng, Y. Qin and C. Li, *ACS Appl. Mater. Interfaces*, 2021, **13**, 39976–39984.

40 L. Song, T. Zhao, D. Yang, X. Wang, X. Hao, Y. Liu, S. Zhang and Z. Z. Yu, *J. Hazard. Mater.*, 2020, **393**, 122332.

41 M. Kalaj, M. S. Denny, K. C. Bentz, J. M. Palomba and S. M. Cohen, *Angew. Chemie*, 2019, **131**, 2358–2362.

42 D. T. Lee, J. Zhao, C. J. Oldham, G. W. Peterson and G. N. Parsons, *ACS Appl. Mater. Interfaces*, 2017, **9**, 44847–44855.

43 D. Gu and F. Schüth, *Chem. Soc. Rev.*, 2014, **43**, 313–344.

44 Y. Ren, Z. Ma and P. G. Bruce, *Chem. Soc. Rev.*, 2012, **41**, 4909–4927.

45 G. Lu, H. Zheng, J. Lv, G. Wang and X. Huang, *J. Power Sources*, 2020, 480, 229091.

46 N. Jaiswal, K. Tanwar, R. Suman, D. Kumar, S. Uppadhya and O. Parkash, *J. Alloys Compd.*, 2019, **781**, 984–1005.

47 A. Trovarelli, *Catal. Rev. - Sci. Eng.*, 1996, **38**, 439–520.

48 M. Mogensen, T. Lindegaard, U. R. Hansen and G. Mogensen, *J. Electrochem. Soc.*, 1994, **141**, 2122.

49 I. Trenque, G. C. Magnano, M. A. Bolzinger, L. Roiban, F. Chaput, I. Pitault, S. Briançon, T. Devers, K. Masenelli-Varlot, M. Bugnet and D. Amans, *Phys. Chem. Chem. Phys.*, 2019, **21**, 5455–5465.

50 J. Ederer, P. Janoš, M. Šťastný, J. Henych, K. Ederer, M. Š. Slušná and J. Tolasz, *J. Environ. Chem. Eng.*, 2021, **9**, 106229.

51 C. Zhao and Y. Xu, *Catal. Today*, 2018, **312**, 141–148.

52 A. Salerno, I. Pitault, T. Devers, J. Pelletier and S. Briançon, *Environ. Toxicol. Pharmacol.*, 2017, **53**, 18–28.

53 D. A. Chen, J. S. Ratliff, X. Hu, W. O. Gordon, S. D. Senanayake and D. R. Mullins, *Surf. Sci.*, 2010, **604**, 574–587.

54 T. Li, R. Tsyshevsky, L. Algrim, M. McEntee, E. Durke, B. Eichhorn, C. Karwacki, M. Zachariah, M. Kuklja and E. Rodriguez, *ACS Appl. Mater. Interfaces*, **13**, 54597–54609.

55 S. C. Laha and R. Ryoo, *Chem. Commun.*, 2003, **3**, 2138–2139.

56 P. Ji, J. Zhang, F. Chen and M. Anpoa, *J. Phys. Chem. C*, 2008, **112**, 17809–17813.

57 T.-W. Kim, F. Kleitz, B. Paul and R. Ryoo, *J. Am. Chem. Soc.*, 2005, **127**, 7601–7610.

58 R. W. Cheary and A. Coelho, *J. Appl. Crystallogr.*, 1992, **2**, 109–121.

59 P. A. DeSario, W. O. Gordon, A. Balboa, A. M. Pennington, C. L. Pitman, M. McEntee and J. J. Pietron, *ACS Appl. Mater. Interfaces*, 2021, **13**, 12550–12561.

60 W. Kohn and L. J. Sham, *Phys. Rev.*, 1965, **140**, 1133–1338.

61 P. Hohenberg and W. Kohn, *Phys. Rev.*, 1964, **136**, 864–871.

62 J. P. Perdew, K. Burke and M. Ernzerhof, *Phys. Rev. Lett.*, 1996, **77**, 3865–3868.

63 P. E. Blöchl, *Phys. Rev. B*, 1994, **50**, 17953–17979.

64 G. Kresse and J. Hafner, *Phys. Rev. B*, 1993, **47**, 558–561.

65 G. Kresse and J. Furthmüller, *Phys. Rev. B - Condens. Matter Mater. Phys.*, 1996, **54**, 11169–11186.

66 G. Kresse and J. Furthmüller, *Comput. Mater. Sci.*, 1996, **6**, 15–50.

67 S. Dudarev and G. Botton, *Phys. Rev. B - Condens. Matter Mater. Phys.*, 1998, **57**, 1505–1509.

68 S. Tosoni and G. Pacchioni, *J. Phys. Chem. C*, 2017, **121**, 28328–28338.

69 S. Grimme, *J. Comput. Chem.*, 2006, **27**, 1787–1799.

70 A. Kundu, G. Piccini, K. Sillar and J. Sauer, *J. Am. Chem. Soc.*, 2016, **138**, 14047–14056.

71 E. Voloshina, *Phys. Rev. B - Condens. Matter Mater. Phys.*, 2012, **85**, 045444.

72 T. Bučko, J. Hafner, S. Lebègue and J. G. Ángyán, *J. Phys. Chem. A*, 2010, **114**, 11814–11824.

73 J. Zang, S. Nair and D. S. Sholl, *J. Phys. Chem. C*, 2013, **117**, 7519–7525.

74 E. N. Voloshina, D. Mollenhauer, L. Chiappisi and B. Paulus, *Chem. Phys. Lett.*, 2011, **510**, 220–223.

75 G. Henkelman, B. P. Uberuaga and H. Jónsson, *J. Chem. Phys.*, 2000, **113**, 9901–9904.

76 E. Paparazzo, *J. Phys. Condens. Matter*, 2018, **30**, 343003.

77 C. Yang, X. Yu, S. Heißler, A. Nefedov, S. Colussi, J. Llorca, A. Trovarelli, Y. Wang and C. Wöll, *Angew. Chemie - Int. Ed.*, 2017, **56**, 375–379.

78 Y. Wang and C. Wöll, *Chem. Soc. Rev.*, 2017, **46**, 1875–1932.

79 R. J. Piffath, *Infrared Spectroscopic Observations on the Fate of Organophosphorus Compounds Exposed to Atmospheric Moisture. Part I. G-Agents and Related Compounds*, 2003.

80 N. Q. Le, G. Bazargan, I. V. Schweigert and D. Gunlycke, *Surf. Sci.*, 2021, **705**, 121765.

81 R. B. Balow, M. McEntee, I. V. Schweigert, S. Jeon, G. W. Peterson and P. Pehrsson, *Langmuir*, 2021, **37**, 6923–6934.

82 A. M. Plonka, Q. Wang, W. O. Gordon, A. Balboa, D. Troya, W. Guo, C. H. Sharp, S. D. Senanayake, J. R. Morris, C. L. Hill and A. I. Frenkel, *J. Am. Chem. Soc.*, 2017, **139**, 599–602.

83 R. Tsyshevsky, S. Holdren, B. W. Eichhorn, M. R. Zachariah and M. M. Kuklja, *J. Phys. Chem. C*, 2019, **123**, 26432–26441.

84 R. Tsyshevsky, A. R. Head, L. Trotochaud, H. Bluhm and M. M. Kuklja, *Surf. Sci.*, 2020, **700**, 121639.

85 D. Ma and Z. Cao, *J. Phys. Chem. C*, 2021, **125**, 24396–24405.

86 Y. M. Choi, H. Abernathy, H. T. Chen, M. C. Lin and M. Liu, *ChemPhysChem*, 2006, **7**, 1957–1963.